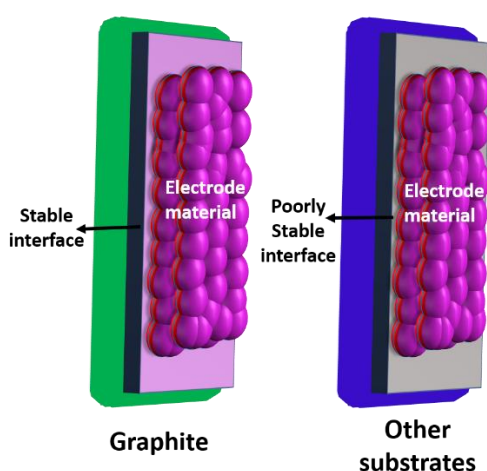


Chapter 3

The Active~Inactive Interface for K^+ Ion Storage~ A Case Study with $Bi_5Nb_3O_{15}$



Understanding the synergy of different fundamental components of a rechargeable aqueous battery is quite pivotal for making technological advances. Herein, we illustrate the aqueous electrolyte enabled electrochemical K^+ ion storage in $Bi_5Nb_3O_{15}$. While achieving a satisfactory electrochemical cycling stability remains a bottleneck, it is countered by establishing a favorable electrochemical interface between the electrode material and current collector.

Ref: R. Baishya and S. K. Das, "Enhanced K^+ ion storage in bismuth niobate ($Bi_5Nb_3O_{15}$) for energy storage and a study on interface," Under revision in Wiley ChemNanoMat, 2025.

3. The Active-Inactive Interface for K^+ Ion Storage- A Case Study with $Bi_5Nb_3O_{15}$

3.1 Introduction

As discussed earlier in the introduction chapter, bismuth-based materials are recently being explored as an electrode material in various rechargeable metal-ion batteries [1,2]. From structural viewpoint, the relatively large interlayer spacing of these materials (i.e. 0.73 nm for $BiOCl$; 0.31 nm for $\beta-Bi_2O_3$) is a boon for the facile transport of charged species in the structure for undergoing electrochemical reactions [3,4]. $Bi_5Nb_3O_{15}$ is an interesting Bi-based material having a layered structure. It has two layers of aurivillous phases: $[(Bi_2O_2)^{2+}(NbO_4)^{3-}]$ and $[(Bi_2O_2)^{2+}(BiNb_2O_7)^-]$ [5,6]. Shu et. al. reported the electrochemical Li^+ ion storage in $Bi_5Nb_3O_{15}$ in non-aqueous electrolyte [7,8]. Like other bismuth-based materials, $Bi_5Nb_3O_{15}$ also suffers from large volume expansion during repeated electrochemical reaction processes which consequently lead to the pulverization of the electrode material [7]. Therefore, various optimization strategies based on morphology, carbon coating and electrolyte design have been proposed to enhance the cycling stability [9].

Another important yet not often discussed component in the evaluation process of K^+ ion system is the choice of current collector. Known as an inactive component, it defines an active-inactive interface with electrode material. There are examples where this interface played a crucial role in significantly enhancing the cycling stability in non-aqueous Li-S or Li^+ ion systems [10-12]. It is even more challenging to select a current collector to work in aqueous environment due to the potential threat of corrosion upon prolonged exposure to the electrolyte [13]. Although much of the research efforts are concentrated on the development of electrode materials for K^+ ion system, there is lack of evidence of the role of the active-inactive interface in defining the electrochemical performance particularly in the aqueous electrolytes. Herein, therefore, considering $Bi_5Nb_3O_{15}$ as a model system, the importance of the interface of the electrode and the current collector in achieving better cycling stability has been illustrated in this chapter.

3.2 Experimental Section

3.2.1 Materials

Bismuth (III) nitrate pentahydrate [$\text{Bi}(\text{NO}_3)_3 \cdot 5\text{H}_2\text{O}$, Merck], acetone, niobium chloride [NbCl_5 , Merck], $\text{NH}_3 \cdot \text{H}_2\text{O}$ and distilled water.

3.2.2 Synthesis

A simple hydrothermal technique was employed to synthesize the bismuth niobate ($\text{Bi}_5\text{Nb}_3\text{O}_{15}$) nanobelts as reported in ref [14]. Concisely, 2.5 mmol of $\text{Bi}(\text{NO}_3)_3 \cdot 5\text{H}_2\text{O}$ and 1.4 mmol of NbCl_5 were dissolved in 10 ml of ethanol separately. The obtained NbCl_5 solution was then transferred to the above $\text{Bi}(\text{NO}_3)_3 \cdot 5\text{H}_2\text{O}$ solution followed by stirring (0.5h). The acidity of the resultant mixture was adjusted to pH 9 by adding $\text{NH}_3 \cdot \text{H}_2\text{O}$ (13 mol L^{-1}) solution. Afterwards, the obtained mixture was stirred vigorously to get a homogeneous mixture of white colour. The white mixture was transferred to a Teflon lined autoclaved and then heated to 200 °C for 24 h. The solution was allowed to cool naturally and then washed several times with distilled water and absolute ethanol. The sample obtained was dried overnight at 80 °C to get the final product.

3.2.3 Characterization

The structural and morphological phase identification of the as prepared $\text{Bi}_5\text{Nb}_3\text{O}_{15}$ was performed using X-ray diffraction (XRD) (BRUKER AXS D8 FOCUS, Cu-K α radiation, $\lambda = 1.5406 \text{ \AA}$), Field emission scanning electron microscopy (FESEM) (Gemini 500) and Fourier transform infra-red spectroscopy (FTIR) (SPECTRUM 100 and FORNTIER IR) techniques. The effect of wettability in the electrochemical mechanism have been investigated by contact angle measurements. The XRD patterns and the crystallographic structure of $\text{Bi}_5\text{Nb}_3\text{O}_{15}$ were indexed with the help of the High score High Score Plus 3.0d (3.0.4) and VESTA Ver. 3.90.1a software respectively.

3.2.4 Electrochemical analysis

The fabrication of the working electrodes has been performed by preparing electrode slurries of $\text{Bi}_5\text{Nb}_3\text{O}_{15}$ using carbon black and PVDF with a weight ratio of 70:20:10 in N-methyl-2-pyrrolidone (NMP) solvent. The prepared slurry was drop casted on titanium (Ti), graphite, stainless steel and nickel current collectors and was dried at 90 °C for 12 h. The electrochemical activity and the charge storage behaviors of the as prepared electrode

material $\text{Bi}_5\text{Nb}_3\text{O}_{15}$ was carried out using cyclic voltammetry (CV) and galvanostatic charge discharge (GCD) measurements in a three-electrode set up. For the three-electrode setup, Pt electrode was used as a counter electrode; whereas the Ag/AgCl electrode was used reference electrode. The cyclic voltammetry and the galvanostatic charge discharge experiments were performed in the working potential window of -1.2 V to 0.3 V (vs Ag/AgCl) at different scan rates. The electrochemical measurements were conducted in 3M KOH electrolyte. The EIS measurements were done in the range of 1 mHz to 200 kHz with a signal amplitude of 10 mV in 3M aqueous KOH electrolyte. The experiments were implemented at room temperature and ambient atmosphere.

3.3 Results and Discussion

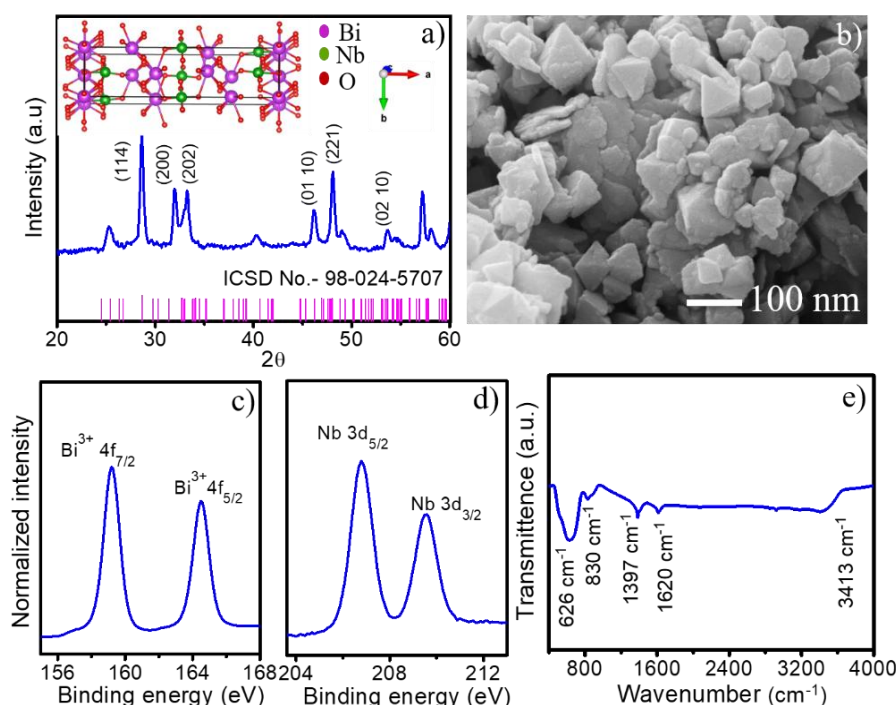


Figure 3.1 a) XRD pattern and crystal structure of $\text{Bi}_5\text{Nb}_3\text{O}_{15}$ (Obtained from VESTA Ver. 3.90.1a), b) FESEM image, XPS spectra of c) Bi 4f and d) Nb 3d in $\text{Bi}_5\text{Nb}_3\text{O}_{15}$ b) FTIR spectrum of $\text{Bi}_5\text{Nb}_3\text{O}_{15}$.

$\text{Bi}_5\text{Nb}_3\text{O}_{15}$ was synthesized hydrothermally and the formation was evaluated using XRD and FTIR analysis. Figure 3.1a shows that the obtained diffraction peaks are consistent with the orthorhombic phase of $\text{Bi}_5\text{Nb}_3\text{O}_{15}$ (ICSD no 98-024-5707) with space group Pnc2. The obtained lattice parameters are $a=21 \text{ \AA}$, $b=5 \text{ \AA}$ and $c=5 \text{ \AA}$. The FESEM micrograph depicts nanosized diamond shaped morphology of $\text{Bi}_5\text{Nb}_3\text{O}_{15}$ (Figure 3.1b). Figure 3.1(c,d) demonstrates the high resolution XPS spectra of $\text{Bi}_5\text{Nb}_3\text{O}_{15}$ [15]. The

obtained doublets at 160 eV and 164 eV corresponds to the binding energies of Bi 4f_{7/2} and Bi 4f_{5/2} electrons of Bi³⁺ oxidation states whereas the O 1s peak can be indexed at 530 eV (Figure 1c and S1d). In addition to that, Nb 3d_{5/2} and Nb 3d_{3/2} binding energy peaks of Nb⁵⁺ state are located at 206 eV and 209 eV (Figure 1d). The FTIR Spectra shows the characteristic bonds according to literature (Figure 3.1e) [7,8, 13-15].

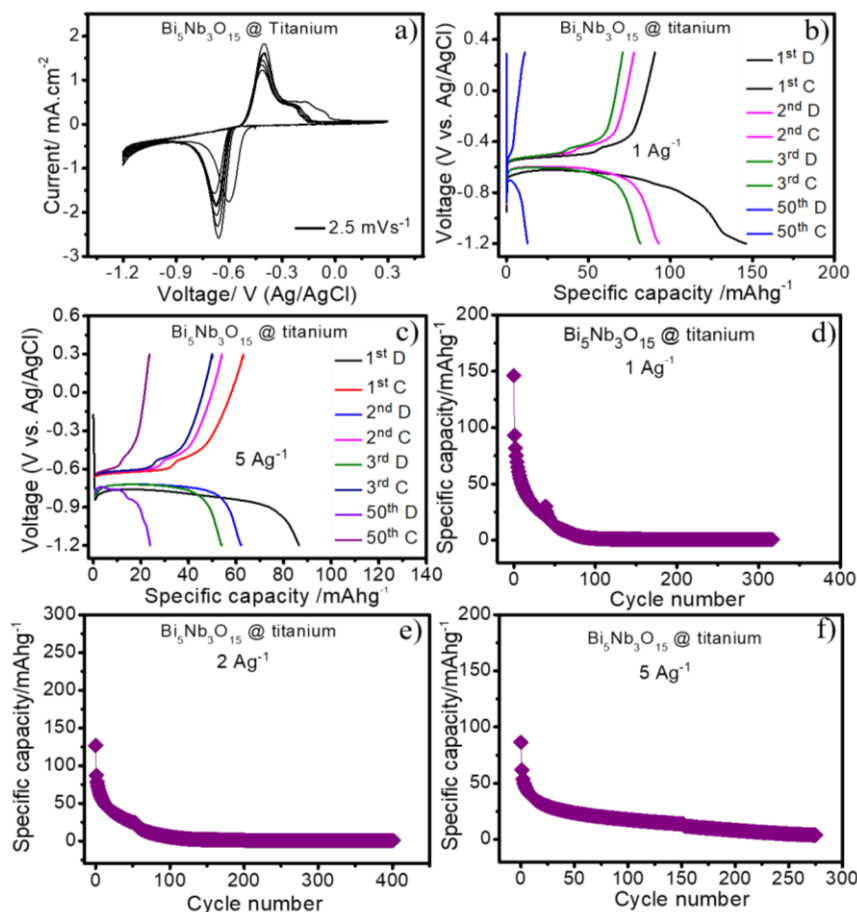


Figure 3.2 (a) Cyclic voltammetry profile at a scan rate of 2.5 mVs⁻¹, GCD profile at a current density of (b) 1 Ag⁻¹, (c) 5 Ag⁻¹, Rate capability at a current density of d) 1 Ag⁻¹ d) 2 Ag⁻¹ d) 5 Ag⁻¹ of Bi₅Nb₃O₁₅ in 3M aqueous KOH electrolyte. The substrate used here is titanium. (D: discharge, C: Charge)

The electrochemical activities of Bi₅Nb₃O₁₅ were examined using the cyclic voltammetry (CV) and galvanostatic charge-discharge (GCD) measurements in the potential window of -1.2 V to 0.3 V (vs Ag/AgCl). Initially, the measurements were carried out in titanium current collector or substrate. Figure 3.2a shows the CV profile of Bi₅Nb₃O₁₅ at a scan rate of 2.5 mVs⁻¹ in 3M aqueous KOH electrolyte. In all the scans, one prominent pair of cathodic and anodic peaks around -0.66 V and -0.41 V. One minor

broad peak around -0.21 V was also noticed. This observation indicates significant redox activity. It is corroborated with the discharge/charge profiles where distinct discharge and charge potential plateaus around -0.68 V and -0.47 V could be noticed (Figure 3.2 (b,c)). The initial discharge and charge capacities are 146 mAhg⁻¹ and 90 mAhg⁻¹ respectively (Fig. 3.2b). However, it is seen that Bi₅Nb₃O₁₅ suffers from severe capacity decline and after 50th cycle, the attained discharge capacity is less than 15 mAhg⁻¹ (Figure 3.2(d-f)). On the other hand, the CV and GCD profiles show slightly different electrochemical behavior with the change of the electrolyte by aqueous 1 M K₂SO₄ and 1 M KCl (Figure 3.3). The cathodic and anodic peaks are shifted to more negative and positive potentials with rapid decrease of current response in subsequent scans (Figure 3.3(a,b)). Similarly, there are no potential plateaus in charge/discharge profiles and the discharge capacity almost reached zero after 15th cycle (Figure 3.3(c-f)).

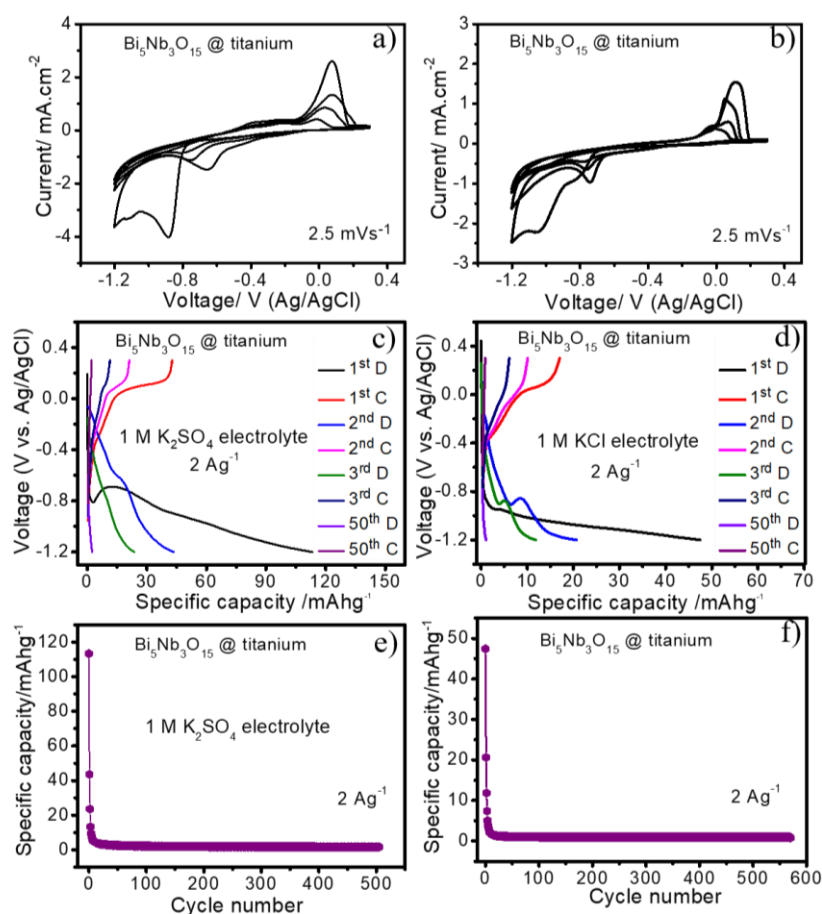


Figure 3.3 Cyclic Voltammetry profile in aqueous a) K₂SO₄ and b) KCl electrolyte at a scan rate of 2.5 mVs⁻¹, Galvanostatic charge-discharge profiles in electrolyte in aqueous c) K₂SO₄ and d) KCl electrolyte; Rate capability in aqueous e) K₂SO₄ and f) KCl at current densities of 2 Ag⁻¹ of Bi₅Nb₃O₁₅. The substrate used here is titanium. (D: discharge, C: Charge)

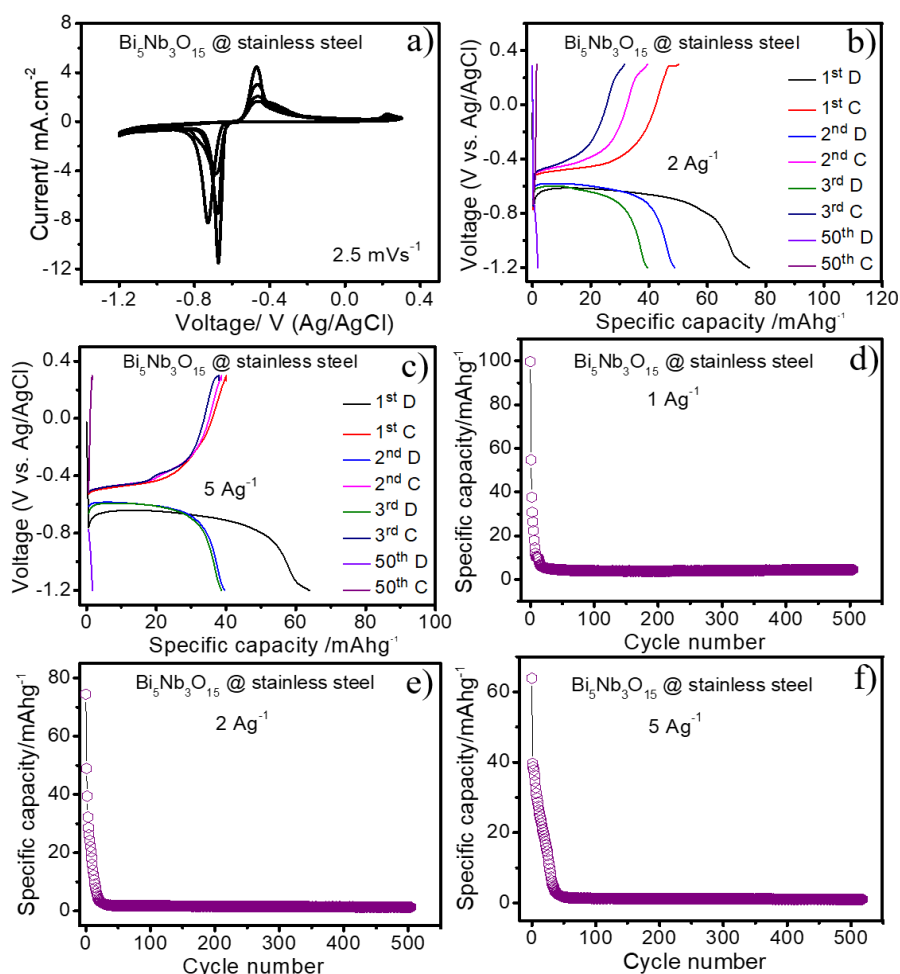


Figure 3.4 (a) Cyclic voltammetry profile at a scan rate of 2.5 mVs^{-1} , Galvanostatic charge discharge profiles at a current density of (b) 2 Ag^{-1} and (c) 5 Ag^{-1} , Rate capability at a current density of d) 1 Ag^{-1} d) 2 Ag^{-1} and e) 5 Ag^{-1} of $\text{Bi}_5\text{Nb}_3\text{O}_{15}$ in 3M aqueous KOH electrolyte. The substrate used here is stainless steel. (D: discharge, C: Charge)

Thereafter, the electrochemical activity of $\text{Bi}_5\text{Nb}_3\text{O}_{15}$ was investigated considering stainless steel as the substrate (Figure 3.4). It is observed that the electrochemical activity in this case is almost similar to the outcomes obtained with titanium under similar experimental conditions. Again, the problem of severe capacity fading prevails since very low discharge capacity of less than 10 mAhg^{-1} was estimated after few cycles (Figure 3.4 (c-f)). Subsequent experimentation with nickel as substrate even shows worst electrochemical performance of $\text{Bi}_5\text{Nb}_3\text{O}_{15}$. Although certain degree of electrochemical activity could be observed around -0.7 V to -0.2 V , there is rapid fall of current response in the negative potential range (Figure 3.5 a). It is again reflected in the charge/discharge

profile where first discharge could not reach the lower cut off potential irrespective of any measured current rates (Figure 3.5 (b,c)).

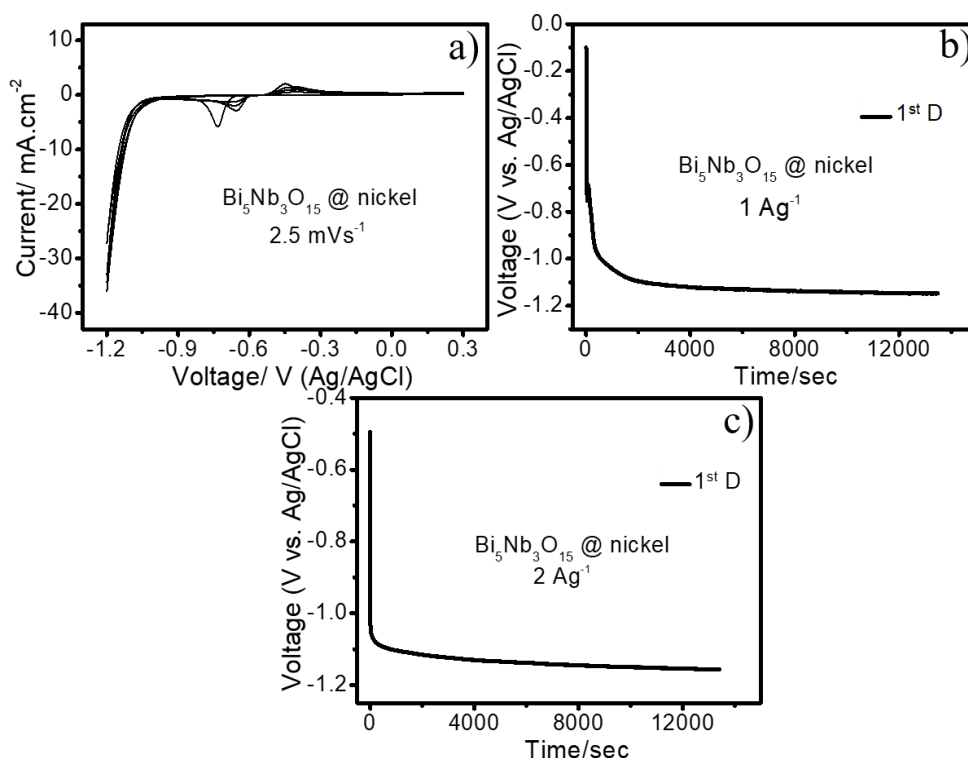


Figure 3.5 a) Cyclic voltammetry profile at a scan rate of 2.5 mVs^{-1} , Galvanostatic charge-discharge profiles of $\text{Bi}_5\text{Nb}_3\text{O}_{15}$ at b) 1 Ag^{-1} and c) 2 Ag^{-1} in 3M aqueous KOH electrolyte. The substrate used here is nickel.

As another alternative substrate, graphite was also explored. It is quite intriguing to notice that this choice could apparently arrest the downfall of specific capacity of $\text{Bi}_5\text{Nb}_3\text{O}_{15}$. As shown in figure 3.5b, a stable discharge capacity of around 110 mAhg^{-1} was achieved after 50th discharge cycle which clearly outperforms the previous discussed results in terms of stability. From the charge/discharge profiles, the discharge plateau at -0.69 V could be observed and three charge plateaus at -0.54 V , -0.44 V and -0.20 V appeared (Figure 3.5b). The similar electrochemical activity is also reflected in the CV profiles (Figure 3.5a). It is important to note here that the minor peaks around -0.27 V and -0.58 V are due to the electrochemical activity of the graphite substrate which was illustrated in the previous chapter [16]. It was also clearly observed that the charge storage capacity of the graphite substrate in KOH electrolytes is very low ($< 10 \text{ mAhg}^{-1}$) at any measured current rates. The rate capability of $\text{Bi}_5\text{Nb}_3\text{O}_{15}$ with graphite substrate is also very impressive. For example, it can sustain a stable storage capacity over 60 mAhg^{-1} at

current rate of 2 Ag^{-1} over 400 cycles (Figure 3.5d). Reckoning graphite as a stable substrate, the electrochemical evaluation of $\text{Bi}_5\text{Nb}_3\text{O}_{15}$ was carried out with K_2SO_4 and KCl electrolytes (Figure 3.7). However, the electrochemical behaviour is found to be quite different in these electrolytes than KOH electrolyte. Not only the distinct discharge and charge plateaus are missing but also there is rapid capacity fading (Figure 3.7 (c-f)). Therefore, it could be commented that there is a synergy of the graphite substrate and the electrolyte in imbining promising electrochemical stability of $\text{Bi}_5\text{Nb}_3\text{O}_{15}$.

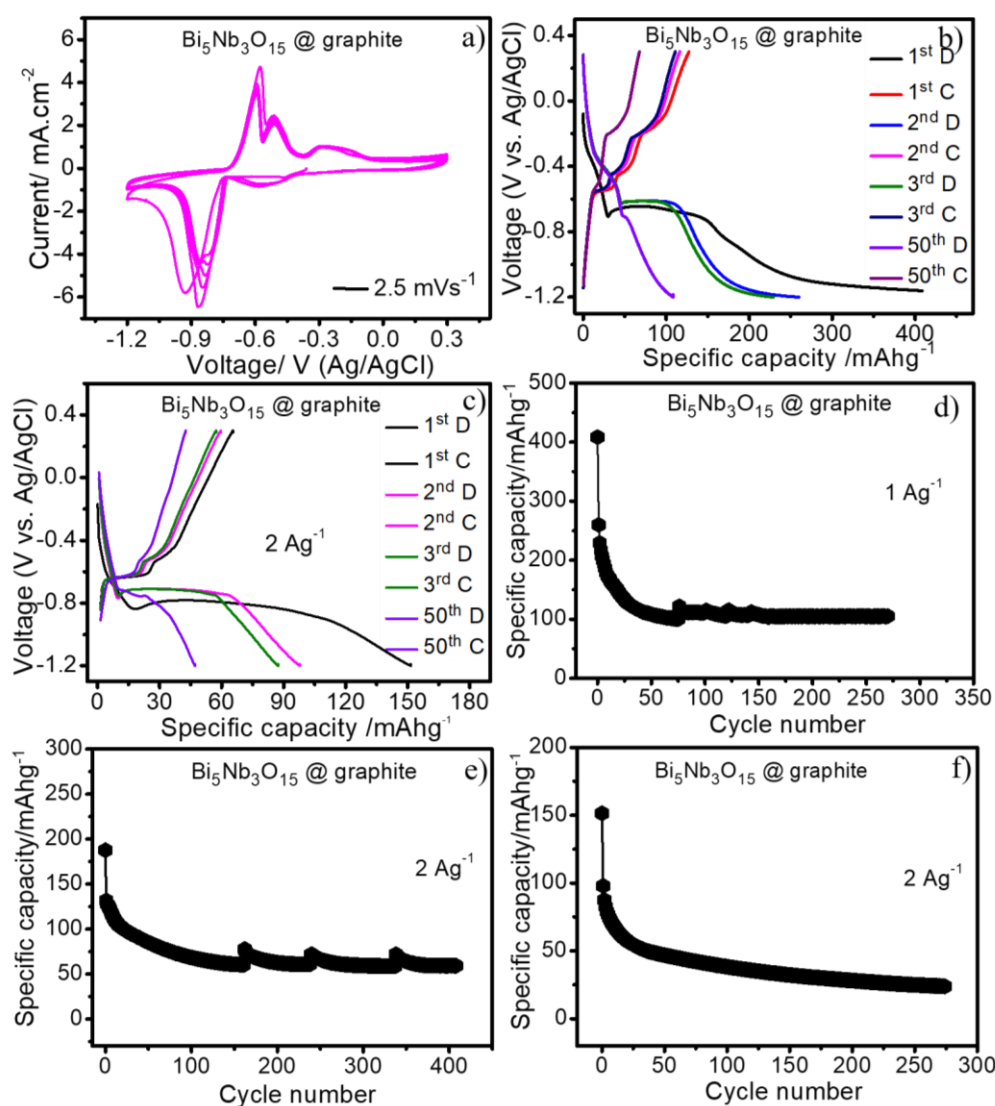


Figure 3.6 (a) Cyclic voltammetry profile at a scan rate of 2.5 mVs^{-1} , Galvanostatic charge-discharge profiles at a current density of (b) 1 Ag^{-1} and (c) 2 Ag^{-1} , Rate capability at a current density of (d) 1 Ag^{-1} , (e) 2 Ag^{-1} and (f) 5 Ag^{-1} of $\text{Bi}_5\text{Nb}_3\text{O}_{15}$. Electrolyte used here is 3 M aqueous KOH electrolyte. The substrate used here is graphite. (D: discharge, C: Charge)

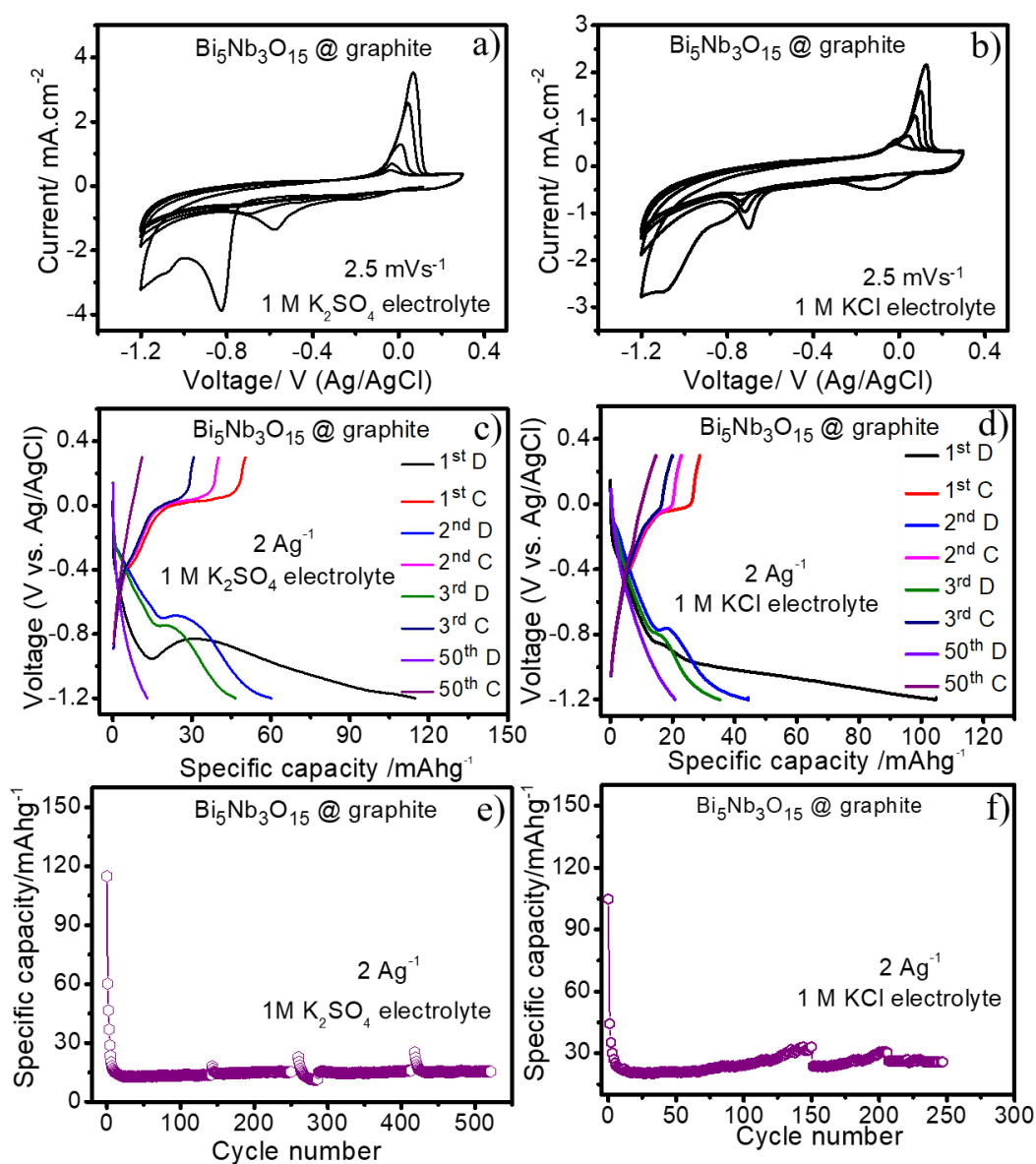


Figure 3.7 Cyclic Voltammetry profiles in aqueous a) K_2SO_4 and b) KCl electrolyte, Galvanostatic charge-discharge profiles in electrolyte in aqueous c) K_2SO_4 and d) KCl electrolyte; Rate capability in aqueous e) K_2SO_4 and f) KCl at current densities of 2 Ag^{-1} of $\text{Bi}_5\text{Nb}_3\text{O}_{15}$. The substrate used here is graphite. (D: discharge, C: charge)

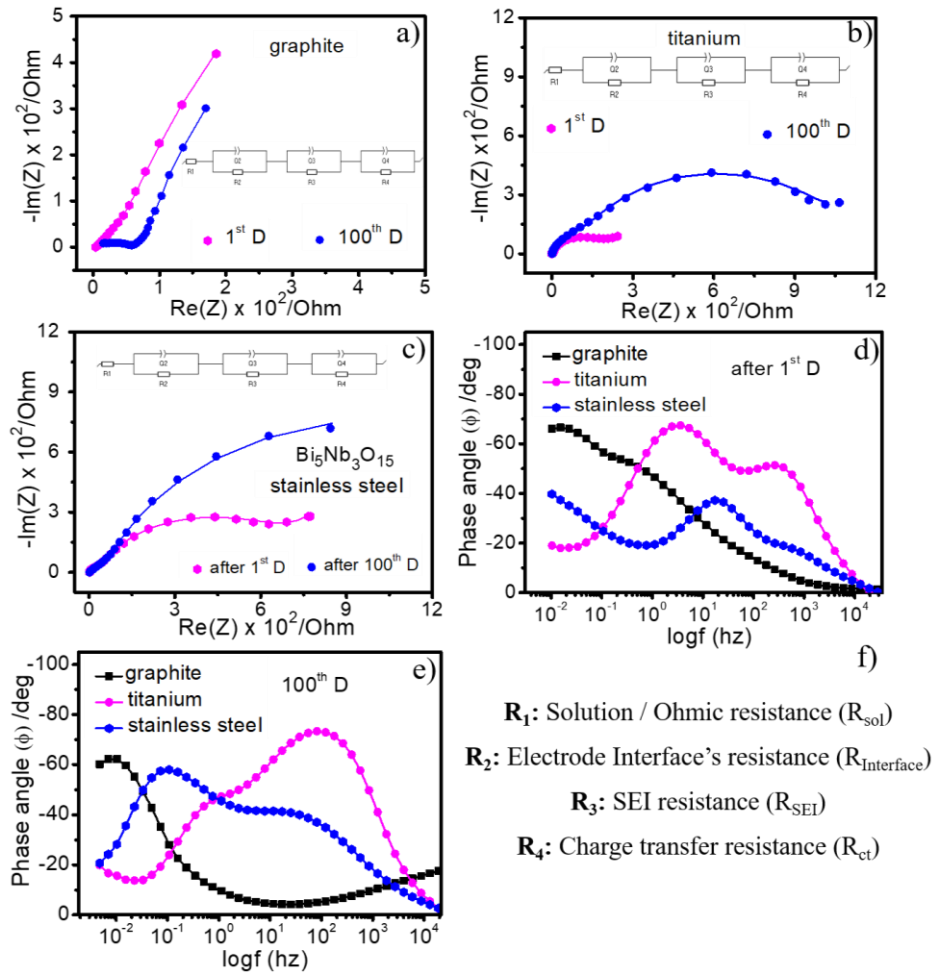


Figure 3.8 Nyquist plots of $\text{Bi}_5\text{Nb}_3\text{O}_{15}$ after 1st D and 100th D on (a) graphite, (b) titanium and (c) stainless steel, bode plot of $\text{Bi}_5\text{Nb}_3\text{O}_{15}$ after (d) 1st D and (e) 100th D on different substrates and (f) fitting parameters. (D: discharge, C: charge)

Sl /No	Substrates with $\text{Bi}_5\text{Nb}_3\text{O}_{15}$	Discharged State	R_1 (Ohm.cm ⁻²)	R_2 (Ohm.cm ⁻²)	R_3 (Ohm.cm ⁻²)	R_4 (Ohm.cm ⁻²)
1	titanium	1D	5.574	350.8	190.6	558.6
		100D	5.574	1092	981.3	1 012
2	stainless steel	1D	5.574	666.5	566.2	740.3
		100D	5.574	2005	1056	1906
3	graphite	1D	5.574	14.96	1911	66.36
		100D	5.574	28.83	1986	77.07

Table 3.1 R_1 , R_2 , R_3 , R_4 values of $\text{Bi}_5\text{Nb}_3\text{O}_{15}$ from the fitted EIS data of figure 3.8 (a-c) in different substrates in aqueous 3 M aqueous KOH electrolyte.

To figure out these contrasting behaviors of $\text{Bi}_5\text{Nb}_3\text{O}_{15}$ in different substrates, EIS measurements were carried out for the 1st and 100th discharged state electrodes. Figure 3.8 (a,b) shows the corresponding Nyquist plots and these are fitted with an equivalent circuit where R_1 , R_2 , R_3 and R_4 represents the solution, electrode interface, SEI, and the charge transfer resistance of the electrode respectively [17,18]. It could be seen that the semicircle in the high frequency region of the 100th discharged electrode is larger in comparison to the 1st discharge electrode for stainless steel and titanium. However, it is noticeably different in case of the graphite substrate. As shown in Table 3.1, it is found that R_2 and R_4 values are significantly high for stainless steel and titanium in comparison to graphite. This signifies that graphite substrate can offer better stability and enhanced reaction kinetics for the electrode material which is also supported by the Bode plots. It is noted that the phase angle can be correlated with the rate of ion transport. The smaller the phase angle value in the lower frequency region means faster ion transport [19]. It is evident from figure 3.8 (c,d) that the phase angle values of $\text{Bi}_5\text{Nb}_3\text{O}_{15}$ in the low frequency region in graphite substrate is smaller than titanium and stainless-steel substrates both for 1st and 100th discharged state electrodes. Another set of time dependent EIS study was carried out with the bare substrates. In this case, the substrates (without $\text{Bi}_5\text{Nb}_3\text{O}_{15}$) were dipped in the electrolyte and EIS spectra were recorded at certain time intervals. Figure 3.9 shows the respective Nyquist plots and the fitted data. The variation of R_2 with time shows that there is significant rise of R_2 values with time for stainless steel, nickel and titanium substrates (Figure 3.9e and Table S₂). However, this value is quite smaller for graphite substrate which hints that it is an important parameter for establishing a better cycling stability of the electrode material (Figure 3.9f and Table 3.2).

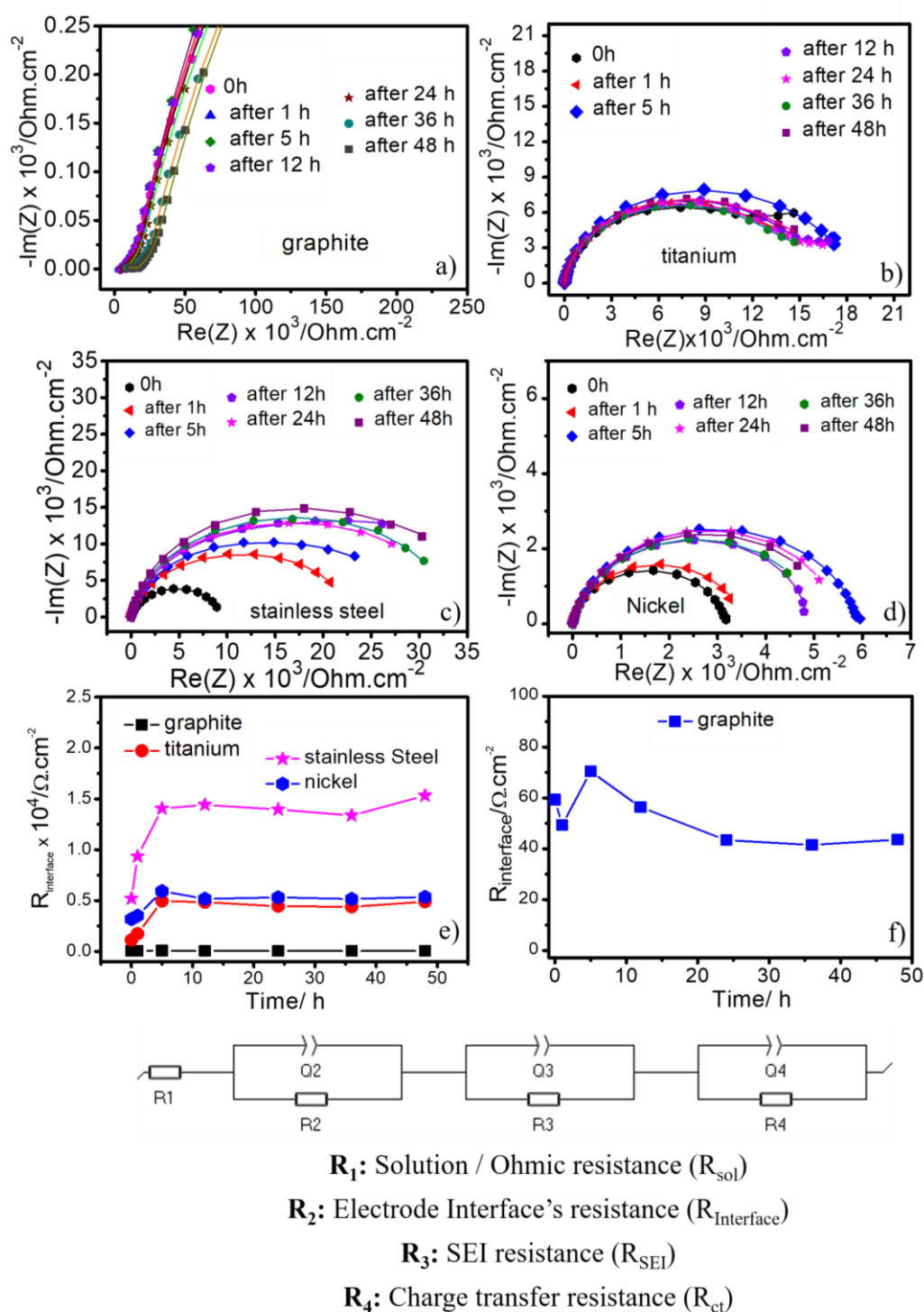


Figure 3.9 Time dependent EIS Nyquist plots of bare (a) graphite, (b) titanium, (c) stainless steel and (d) nickel substrates, (e) $R_{\text{interface}}$ vs time plot for different bare substrates after certain time intervals, (f) enlarged view of $R_{\text{interface}}$ vs time for natural graphite. (D: discharge, C: charge) (fitting parameters enclosed).

Sl/ No	Substrates	Time frame	R_{sol} ($\Omega \cdot \text{cm}^{-2}$)	$R_{interface}$ ($\Omega \cdot \text{cm}^{-2}$)	R_{SEI} ($\Omega \cdot \text{cm}^{-2}$)	R_{ct} ($\Omega \cdot \text{cm}^{-2}$)
1	graphite	0h	5.574	59.34	1977	8.692
		1h	5.574	49.27	3327	7.658
		5h	5.574	70.46	4013	8.26
		12h	5.574	56.32	4047	6.884
		24h	5.574	43.38	5196	6.581
		36h	5.574	41.52	5574	10.43
		48h	5.574	43.63	5571	10.17
2	titanium	0h	5.574	1130	12110	12490
		1h	5.574	1733	13070	15285
		5h	5.574	4968	14079	16322
		12h	5.574	4843	15081	15761
		24h	5.574	4450	15702	15777
		36h	5.574	4382	15668	15741
		48h	5.574	4888	15594	15805
3	stainless steel	0h	5.574	5208	248.37	3995
		1h	5.574	9344	547.6	16460
		5h	5.574	14052	1334	16586
		12h	5.574	14400	1406	16996
		24h	5.574	13953	1496	20341
		36h	5.574	13364	1514	19733
		48h	5.574	15317	2185	19969
4	nickel	0h	5.574	3182	947.3	3195
		1h	5.574	3515	1389	3628
		5h	5.574	5921	1373	5605
		12h	5.574	5177	2515	5420
		24h	5.574	5301	2832	5766
		36h	5.574	5162	4821	9534
		48h	5.574	5360	5232	9560

Table 3.2 Time dependent R_1 , R_2 , R_3 , R_4 values of bare substrates from the fitted EIS data of figure 3.9. Electrolytes used here is aqueous 3M aqueous KOH electrolyte.

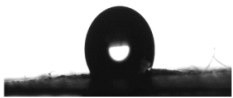


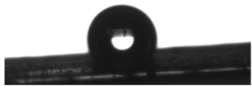
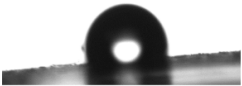
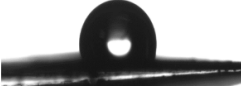
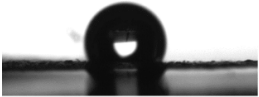
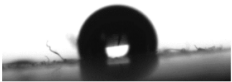
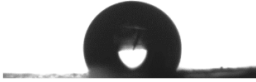
	before discharge	after 1 st D	after 100 th D
Bi ₅ Nb ₃ O ₁₅ @ graphite	 114°	 101.4°	 49.6°
Bi ₅ Nb ₃ O ₁₅ @titanium	 114.5°	 100.1°	 104°
Bi ₅ Nb ₃ O ₁₅ @stainless steel	 113.9°	 113.9°	 113.9°

Figure 3.10. Change in contact angle values of Bi₅Nb₃O₁₅ before and after 1st, 100th discharge state electrode in graphite, titanium and stainless-steel substrate.

Sl/ no	Substrates with Bi ₅ Nb ₃ O ₁₅	Pristine Bi ₅ Nb ₃ O ₁₅ (before discharge)	After 1 st D	After 100 th D
1	graphite	114°	101.4°	49.6°
2	titanium	122.3°	92.1°	104°
3	stainless steel	112.9°	106.2°	105.2°

Table 3.3. Contact angle values of Bi₅Nb₃O₁₅ for different substrates after before, 1st and 100th discharge state electrode.

Sl/ no	Substrates with Bi ₅ Nb ₃ O ₁₅	1D (V)	1C (V)	Difference (V)	2D (V)	2C (V)	Difference (V)
1	graphite	-0.8	-0.62	0.18	-0.71	-0.63	0.08
2	titanium	-0.77	-0.60	0.17	-0.73	-0.58	0.15
3	stainless steel	-0.67	-0.5	0.17	-0.6	-0.44	0.16

Table 3.4. Overpotential of Bi₅Nb₃O₁₅ after 1st and 2nd discharge. (D: discharge, C: charge)

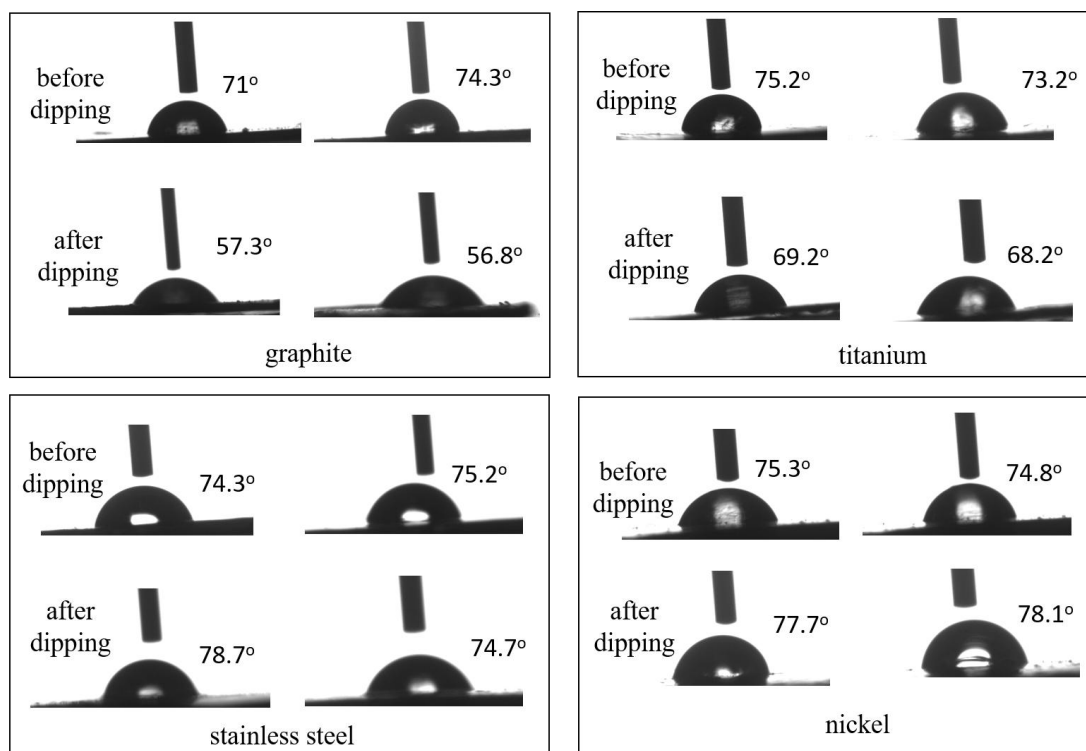


Figure 3.11 Contact angle values for bare graphite, titanium, stainless steel and nickel substrates without $\text{Bi}_5\text{Nb}_3\text{O}_{15}$ before and after dipping. (repeated two times)

Sl/ no	Bare Substrates	Before dipping	After dipping
1	graphite	71°/74.3°	57.3°/56.8°
2	titanium	75.2°/73.2°	69.2°/68.2°
3	stainless steel	74.3°/75.2°	78.7°/74.7°
4	nickel	75.3°/74.8°	77.7°/78.1°

Table 3.5. Contact angle values of different substrates without $\text{Bi}_5\text{Nb}_3\text{O}_{15}$ before and after dipping in KOH electrolyte.

The process of electrowetting plays a crucial role in the determination of the electrode performance. For a better understanding, contact angle measurements were conducted on the pristine $\text{Bi}_5\text{Nb}_3\text{O}_{15}$ electrode before discharge and after 1st and 100th discharged state electrodes using water as solvent. It is found that the contact angle of the $\text{Bi}_5\text{Nb}_3\text{O}_{15}$ on graphite substrate decreases significantly after 100th discharge cycle, whereas no such changes were noticeable for other substrates (Figure 3.10 and Table 3.3).

It may be inferred that the enhancement in the wettability of $\text{Bi}_5\text{Nb}_3\text{O}_{15}$ with time on the graphite substrate is related to an improved electrode-electrolyte interaction which may subsequently result in the reduced interfacial resistance as evidenced from figure 3.10. The decreased contact angle value may also indicate a reduction in the overpotential to drive K^+ ion insertion in the electrode material [20]. Table 3.4 indicates reduced overpotential for graphite substrate from second cycle onwards. Additionally, it is also found that there is a reduction (approximately by 15%) of the contact angle of the bare graphite substrate after soaking it in the electrolyte for 48 h (Figure 3.11 and Table 3.5). This is not the case for the other three bare substrates. It hints that even the wettability of the pristine graphite substrate improves significantly over time. A careful inspection of the FESEM images of the pristine graphite and graphite dipped in the electrolyte for 48 h indicates a change of the overall roughness, which is otherwise not so prominently evident for other substrates (Figure 3.12).

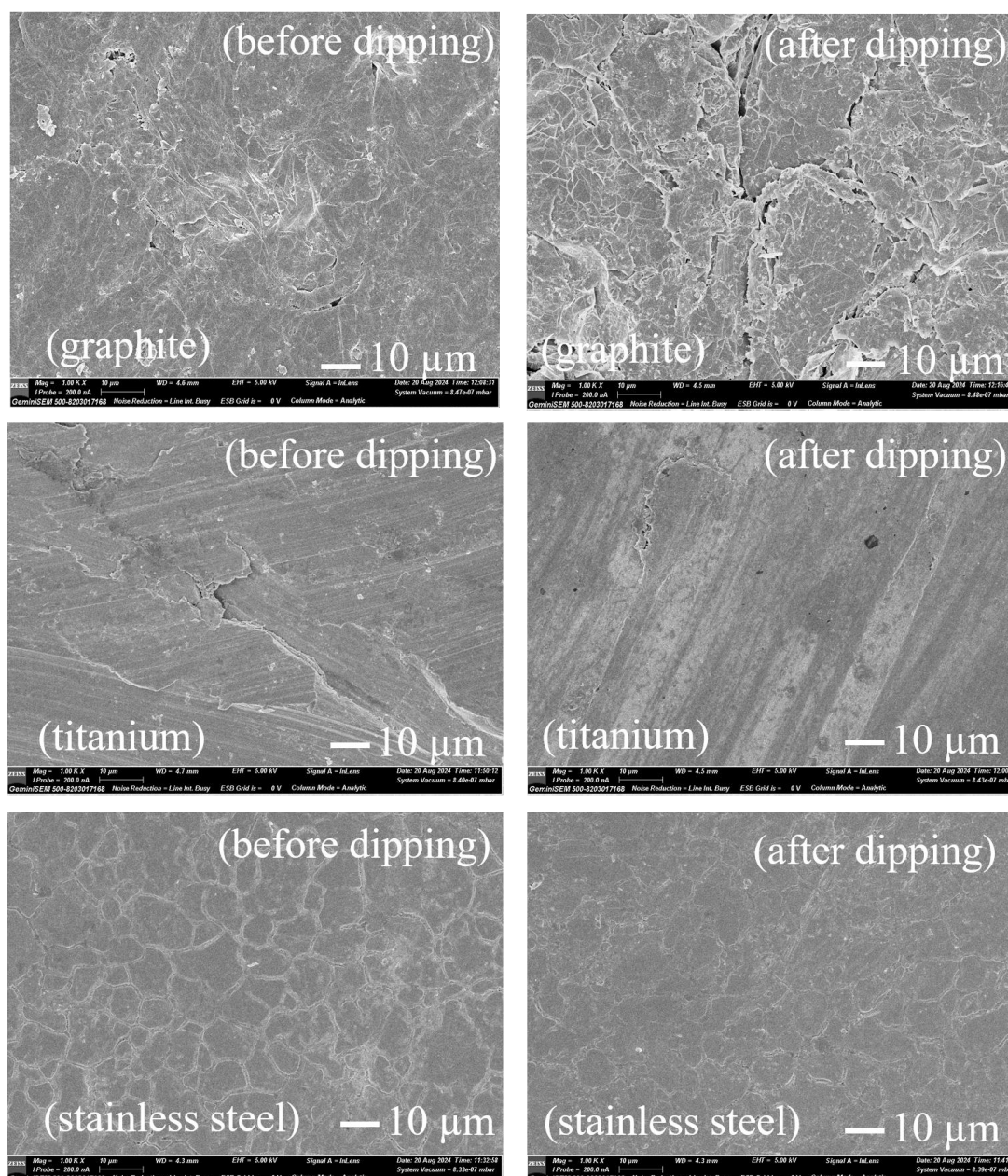


Figure 3.12. FESEM images of bare graphite, titanium and stainless steel before and after dipping in KOH electrolyte.

Furthermore, in an attempt to better understand the stability of the current collectors, polarization behaviors were analyzed, which were obtained from LPR measurement [21,22]. The obtained polarization data near the polarization potential was fitted using Tafel extrapolation techniques. It is seen from figure 3.13 (a,e) that graphite shows the most positive shift in corrosion potential. The corrosion potential for nickel found to be on the higher negative side among all substrates (Figure 3.13(d,e)). The corrosion rate and the polarization resistance (R_p) were obtained using the fitted polarization profiles (Figure

3.13f and Table 3.6). It is observed that the corrosion rate is highest in case of nickel current collector whereas graphite shows the lowest corrosion rate. Supporting it, the R_p value is much higher in case of the graphite in comparison to the others (Table 3.6).

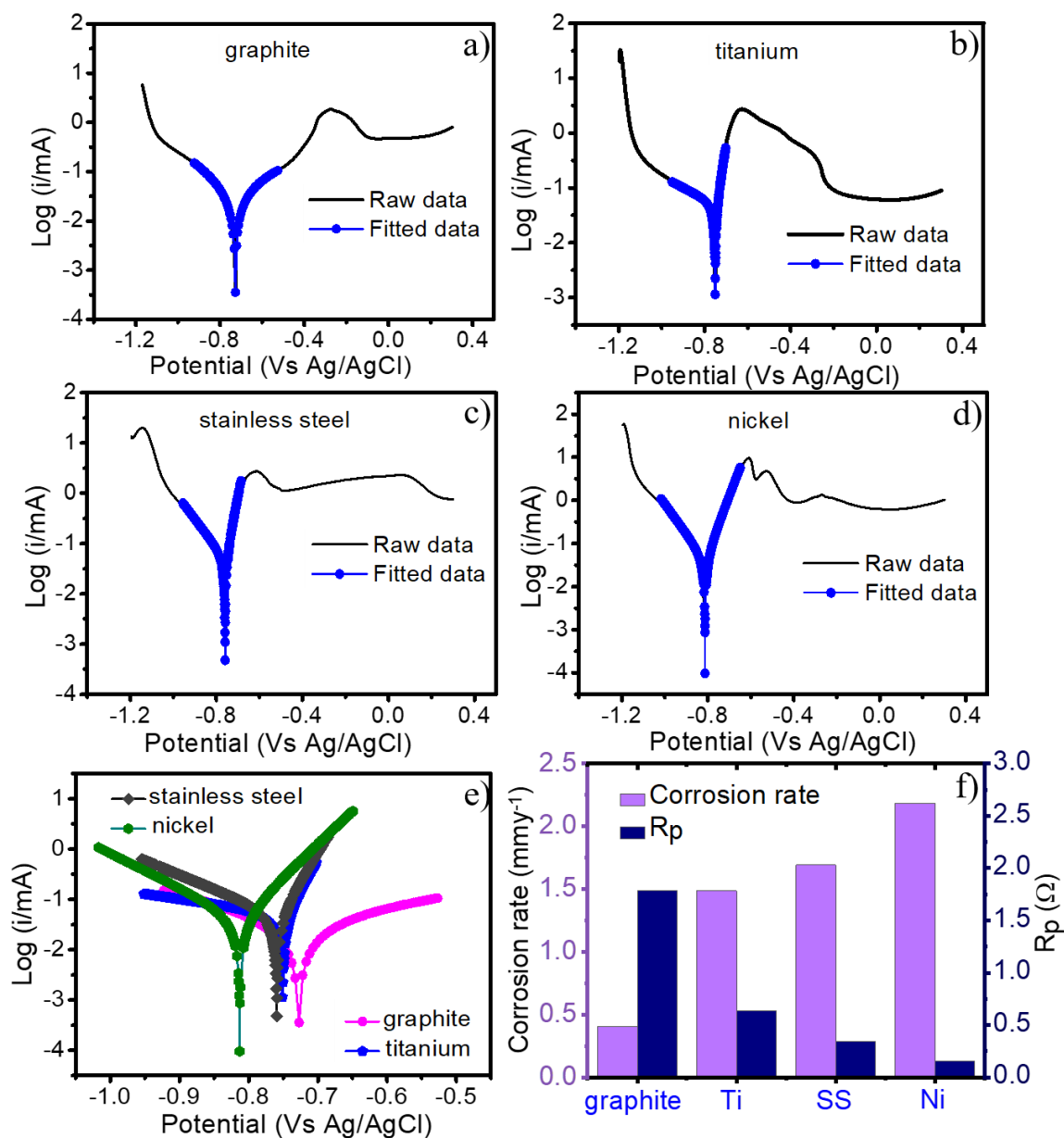


Figure 3.13 Corrosion potential for (a) graphite, (b) titanium, (c) stainless steel and (d) nickel substrates, e) Fitted Tafel extrapolation plots of different current collectors, f) Comparison of corrosion rates and polarization resistances (R_p) calculated by fitting in the EC lab software.

Sl/ no	Current collector	E _{Corrosion} (mV)	I _{Corrosion} (μ A)	β_a (mV)	β_c (mV)	R _p (Ω)	Corrosion rate (mmy ⁻¹)
1	graphite	-728.01	23.282	78.9	195.3	1786	0.404
2	titanium	-755.886	96.221	123.5	303.0	637	1.488
3	stainless steel	-760.456	48.639	123.1	175.7	347	1.692
4	nickel	-814.00	204.391	178.6	348.7	155	2.185

Table 3.6. Different parameters obtained from extrapolation of Tafel plot.

In order to understand the charge storage mechanism, postmortem studies were carried out using different ex-situ characterization techniques. Figure 3.14 (a-c) compares the XRD patterns of the discharged and charged state $\text{Bi}_5\text{Nb}_3\text{O}_{15}$ electrodes with the pristine $\text{Bi}_5\text{Nb}_3\text{O}_{15}$. It could be seen that the diffraction peaks shift toward the higher angle after the 1st discharge. For example, the (114) and (221) peaks positioned at 28.63° and 48.1° are shifted by 0.17° and 0.13° respectively. Similar kind of shift was also observed for the 1st charged state electrode. However, there is a difference. First, the (221) peak regains its original position and (200) peak completely disappeared. But there is complete loss of crystallinity of the electrode material after 100 cycles signifying either formation of amorphous or nanocrystalline state. These kind of amorphization may be interlinked with the achieved material stability [23]. Although FESEM images after 1st discharge and 1st charge show almost similar morphological state like the pristine $\text{Bi}_5\text{Nb}_3\text{O}_{15}$, but the electrode material exhibit disintegration after 100 cycles (Figure 3.14 (d,e)). Similarly, a comparison of the FTIR spectra of the pristine $\text{Bi}_5\text{Nb}_3\text{O}_{15}$ and discharged-charged states electrodes are shown in figure 3.15 (a,b). The peak positioned at 620 cm^{-1} corresponds to the Nb-O stretching of the terminal oxygen in the group vibration of NbO_6 octahedra, whereas the peak around 510 cm^{-1} and 820 cm^{-1} can be ascribed to the bonding vibration of Bi-O bond [24,25]. A weak absorption peak around 3400 cm^{-1} and a peak around 1620 cm^{-1} can also be indexed with the stretching and bending of O-H bond in the absorbed water molecule by the sample [26]. Interestingly, some new peaks in the range of $850\text{--}900\text{ cm}^{-1}$ and $1000\text{--}1200\text{ cm}^{-1}$ are seen in the discharged state electrodes which could be ascribed to the Bi-O-Bi stretching and the BiO_6 octahedral stretching vibration [27]. Again, the peak near 510 cm^{-1} disappeared in the discharged state electrodes hinting breaking of the Bi-O bond during cycling. Moreover, while the obtained XPS spectra of the discharged

state electrode does not show prominent change with respect to the pristine $\text{Bi}_5\text{Nb}_3\text{O}_{15}$, it shows the presence of K2p peaks which depicts insertion of K species during cycling (Figure 3.16b and (c-e)).

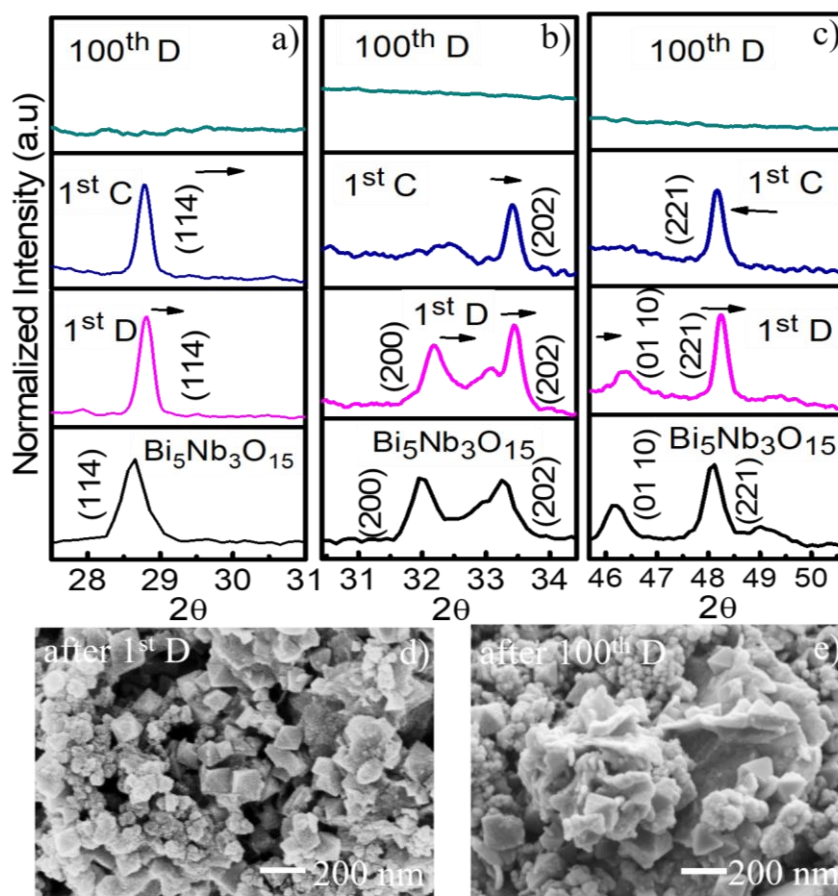


Figure 3.14 (a-c) Ex-situ XRD analysis before and after 1st D, 1st C, and 100th D state electrodes, Ex-situ FESEM images after d) 1st D, and e) 100th D state electrode. (D: discharge, C: charge)

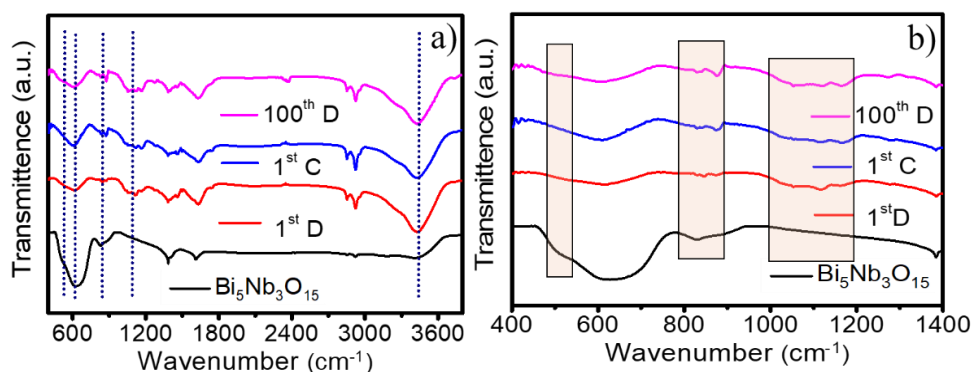


Figure 3.15 (a,b) FTIR analysis of before and after discharged state electrodes. (D: discharge, C: charge)

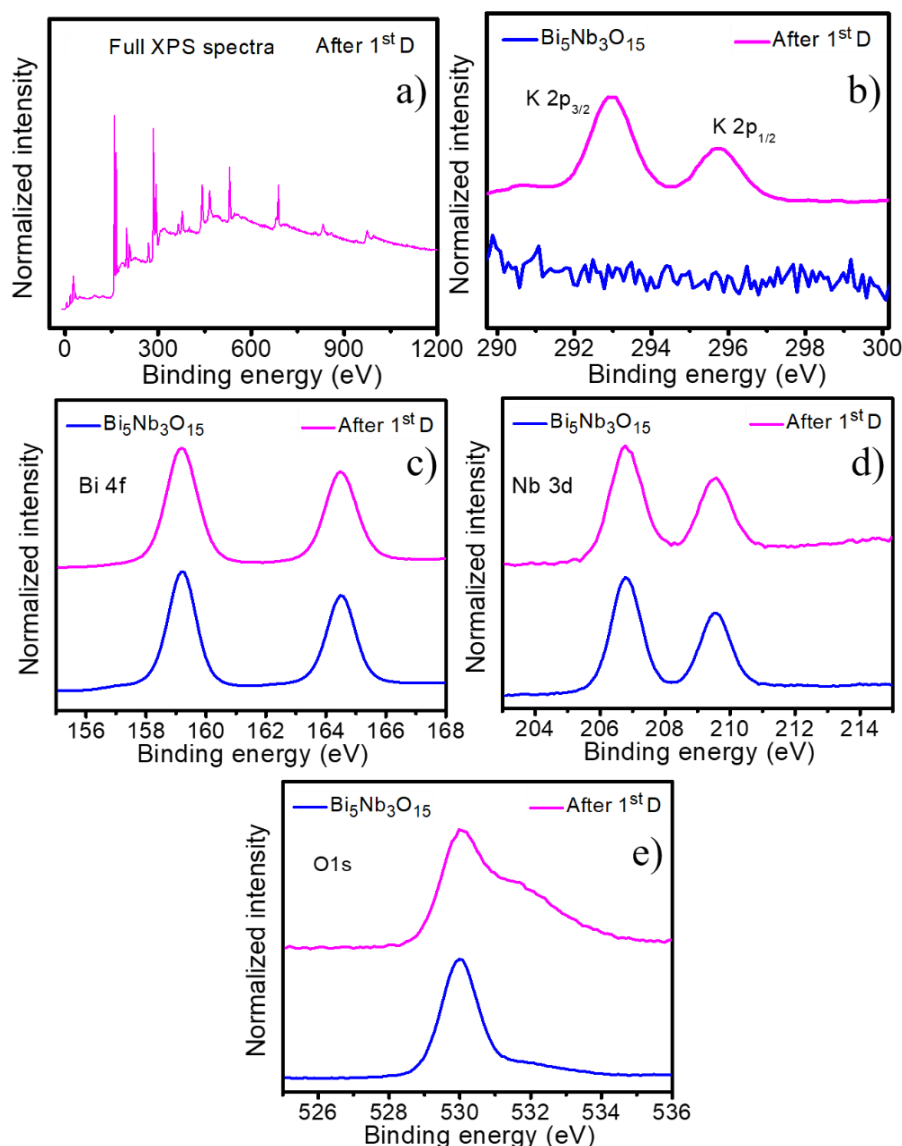


Figure 3.16 Ex-situ XPS spectra of (a) Full spectra, (b) K2p, (c) Bi4f, (d) Nb3d and (e) O1s in discharged state electrode of $\text{Bi}_5\text{Nb}_3\text{O}_{15}$. (D: discharge, C: charge)

3.4 Conclusion

In summary, the electrochemical K^+ ion storage in the aurivillous phase $\text{Bi}_5\text{Nb}_3\text{O}_{15}$ in aqueous electrolyte is discussed for the first time. Although rapid capacity fading was witnessed in initial assessments, the use of graphitic current collector helps in mitigating the issue. A study of the interface of the electrode material and the different current collectors shows that the interface resistance plays a crucial role in determining the electrochemical performance of $\text{Bi}_5\text{Nb}_3\text{O}_{15}$. The graphite substrates shows less interface resistance which reflects in the better cycling stability of $\text{Bi}_5\text{Nb}_3\text{O}_{15}$. The contact angle

measurements hint the significant role of wettability in driving enhanced electrochemical reaction which basically gives a stable cycling behavior of the material.

3.5 References

- [1] Qian, H., Liu, Y., Chen, H., Feng, K., Jia, K., Pan, K., Wang, G., Huang, T., Pang, X. and Zhang, Q. Emerging bismuth-based materials: From fundamentals to electrochemical energy storage applications. *Energy Storage Materials*, 58: 232-270, 2023.
- [2] Xu, K., Wang, L., Xu, X., Dou, S.X., Hao, W. and Du, Y. Two-dimensional bismuth-based layered materials for energy-related applications. *Energy Storage Materials*, 19: 446-463, 2019.
- [3] Liang, Y.C. and Chou, Y.H. Improved photoelectrode performance of chemical solution-derived Bi₂O₃ crystals via manipulation of crystal characterization. *RSC advances*, 10(73): 45042-45058, 2020.
- [4] Ye, L., Liu, J., Gong, C., Tian, L., Peng, T. and Zan, L. Two different roles of metallic Ag on Ag/AgX/BiOX (X= Cl, Br) visible light photocatalysts: surface plasmon resonance and Z-scheme bridge. *Acs Catalysis*, 2(8): 1677-1683, 2012.
- [5] Bian, W., Wang, Y., Yang, H., Li, P., Yu, Q., Shuang, S., Dong, C. and MF Choi, M. A fluorescent probe using the boron and nitrogen co-doped carbon dots for the detection of Hg²⁺ ion in environmental water samples. *Current Analytical Chemistry*, 13(3): 242-249, 2017.
- [6] Depablos-Rivera, O., Medina, J.C., Bizarro, M., Martínez, A., Zeinert, A. and Rodil, S.E. Synthesis and properties of Bi₅Nb₃O₁₅ thin films prepared by dual co-sputtering. *Journal of Alloys and Compounds*, 695: 3704-3713, 2017.
- [7] Li, Y., Zheng, R., Yu, H., Cheng, X., Liu, T., Peng, N., Zhang, J., Shui, M. and Shu, J. Fabrication of one-dimensional architecture Bi₅Nb₃O₁₅ nanowires by electrospinning for lithium-ion batteries with enhanced electrochemical performance. *Electrochimica Acta*, 299: 894-901, 2019.

-
- [8] Li, Y., Zheng, R., Yu, H., Cheng, X., Zhu, H., Bai, Y., Liu, T., Shui, M. and Shu, J. Carbon-coated $\text{Bi}_5\text{Nb}_3\text{O}_{15}$ as anode material in rechargeable batteries for enhanced lithium storage. *Ceramics International*, 44(10): 11505-11511, 2018.
- [9] Zhou, X., Chen, X., Kuang, W., Zhang, X., Wu, X., Chen, X., Zhang, C., Li, L. and Chou, S. Strategies to boost the electrochemical performance of bismuth anode for potassium-ion batteries. *Chemical Science*: 2024.
- [10] Luo, L., Chung, S.H., Chang, C.H. and Manthiram, A. A nickel-foam@ carbon-shell with a pie-like architecture as an efficient polysulfide trap for high-energy Li-S batteries. *Journal of Materials Chemistry A*, 5(29): 15002-15007, 2017.
- [11] Zhang, Y., Jing, S., Shen, H., Li, S., Huang, Y., Shen, Y., Liu, S., Zhang, Z. and Liu, F. Developments, Novel Concepts, and Challenges of Current Collectors: From Conventional Lithium Batteries to All-Solid-State Batteries. *ChemElectroChem*, 11(14): 202300739, 2024.
- [12] Naskar, P., Saha, A., Biswas, B. and Banerjee, A. Current Collectors for Rechargeable Batteries: State-of-the-Art Design and Development Strategies for Commercial Products. *Journal of The Electrochemical Society*, 171(1): 010515, 2024.
- [13] Liu, B., Lv, T., Zhou, A., Zhu, X., Lin, Z., Lin, T. and Suo, L. Aluminum corrosion-passivation regulation prolongs aqueous batteries life. *Nature Communications*, 15(1): 2922, 2024.
- [14] Guo, Y., Chen, L., Yang, X., Ma, F., Zhang, S., Yang, Y., Guo, Y. and Yuan, X. Visible light-driven degradation of tetrabromobisphenol A over heterostructured $\text{Ag/Bi}_5\text{Nb}_3\text{O}_{15}$ materials. *RSC Advances*, 2(11): 4656-4663, 2012.
- [15] Zhang, S., Yang, Y., Guo, Y., Guo, W., Wang, M., Guo, Y. and Huo, M., 2013. Preparation and enhanced visible-light photocatalytic activity of graphitic carbon nitride/bismuth niobate heterojunctions. *Journal of hazardous materials*, 261: 235-245, 2013.
- [16] Baishya, R., Sarmah, D., Mahanta, D. and Das, S.K. Aqueous electrolyte-mediated reversible K^+ ion insertion into graphite. *Physical Chemistry Chemical Physics*, 25(36): 24298-24302, 2023.
-

- [17] Nugroho, A.P., Hawari, N.H., Prakoso, B., Refino, A.D., Yulianto, N., Iskandar, F., Kartini, E., Peiner, E., Wasisto, H.S. and Sumboja, A. Vertically aligned n-type silicon nanowire array as a free-standing anode for lithium-ion batteries. *Nanomaterials*, 11(11): 3137, 2021.
- [18] Han, S.D., Kim, S., Li, D., Petkov, V., Yoo, H.D., Phillips, P.J., Wang, H., Kim, J.J., More, K.L., Key, B. and Klie, R.F. Mechanism of Zn insertion into nanostructured δ -MnO₂: a nonaqueous rechargeable Zn metal battery. *Chemistry of Materials*, 29(11): 4874-4884, 2017.
- [19] Wang, D.W., Li, F., Fang, H.T., Liu, M., Lu, G.Q. and Cheng, H.M. Effect of pore packing defects in 2-D ordered mesoporous carbons on ionic transport. *The Journal of Physical Chemistry B*, 110(17): 8570-8575, 2006.
- [20] Hu, X., Borowiec, J., Zhu, Y., Liu, X., Wu, R., Ganose, A.M., Parkin, I.P. and Boruah, B.D. Dendrite-Free Zinc Anodes Enabled by Exploring Polar-Face-Rich 2D ZnO Interfacial Layers for Rechargeable Zn-Ion Batteries. *Small*, 20(18): 2306827, 2024.
- [21] Naskar, P., Mandal, S., Banerjee, D., Dey, A., Dinda, I., Maiti, M., Mondal, S. and Banerjee, A. Exploring the prospects of potassium vanadate as a negative electrode in an aqueous Al-ion gel battery with copper-Prussian blue analogue positive electrode for solar applications. *Ionics*: 1-16, 2025.
- [22] Unal, B., Sel, O. and Demir-Cakan, R. Current collectors' corrosion behaviours and rechargeability of TiO₂ in Aqueous Electrolyte Aluminium-ion batteries. *Journal of Applied Electrochemistry*, 54(6): 1425-1434, 2024.
- [23] Nandi, S., Sonigara, K. K. and Pumera, M. Exploring the electrochemistry of Al³⁺ ion in amorphous Bi₄V₂O₁₁ for rechargeable aqueous aluminum-ion battery. *Applied Materials Today*, 42: 102568, 2025.
- [24] Li, Y., Zheng, R., Yu, H., Cheng, X., Liu, T., Peng, N., Zhang, J., Shui, M. and Shu, J. Fabrication of one-dimensional architecture Bi₅Nb₃O₁₅ nanowires by electrospinning for lithium-ion batteries with enhanced electrochemical performance. *Electrochimica Acta*, 299: 894-901, 2019.

- [25] Zhang, S., Yang, Y., Guo, Y., Guo, W., Wang, M., Guo, Y. and Huo, M. Preparation and enhanced visible-light photocatalytic activity of graphitic carbon nitride/bismuth niobate heterojunctions. *Journal of hazardous materials*, 261: 235-245, 2013.
- [26] Kuźniarska-Biernacka, I., Silva, A.R., Carvalho, A.P., Pires, J. and Freire, C. Organo-laponites as novel mesoporous supports for manganese (III) salen catalysts. *Langmuir*, 21(23): 10825-10834, 2005.
- [27] Hossain, M.Z., Nishat, S.S., Ahmed, S., Hossain, Q.S., Khan, M.N.I., Hasan, T., Bashar, M.S., Faysal, A.S.H., Syed, I.M., Hossain, K.S. and Hussain, S. Combined experimental and DFT approach to BiNbO₄ polymorphs. *RSC advances*, 13(8): 5576-5589, 2023.